

PAPER

An optoelectronic notch ('dip') phenomenon in the heterodyne photocarrier radiometry frequency response of Si wafers: a route to quantitative trap-state dynamic processes in semiconductors

Recent citations

- [Quantitative Imaging of Defect Distributions in CdZnTe Wafers Using Combined Deep-Level Photothermal Spectroscopy, Photocarrier Radiometry, and Lock-In Carrierography](#)
Alexander Melnikov *et al*

To cite this article: Yaqin Song *et al* 2020 *Semicond. Sci. Technol.* **35** 115024

View the [article online](#) for updates and enhancements.



The Electrochemical Society
Advancing solid state & electrochemical science & technology

The ECS is seeking candidates to serve as the
Founding Editor-in-Chief (EIC) of ECS Sensors Plus,
a journal in the process of being launched in 2021

The goal of ECS Sensors Plus, as a one-stop shop journal for sensors, is to advance the fundamental science and understanding of sensors and detection technologies for efficient monitoring and control of industrial processes and the environment, and improving quality of life and human health.

Nomination submission begins: May 18, 2021



Nominate now!

An optoelectronic notch ('dip') phenomenon in the heterodyne photocarrier radiometry frequency response of Si wafers: a route to quantitative trap-state dynamic processes in semiconductors

Yaqin Song^{1,2}, Andreas Mandelis^{2,3,4}, Alexander Melnikov²  and Qiming Sun^{2,3} 

¹ School of Aerospace, Xi'an Jiaotong University, Xi'an 710049, People's Republic of China

² Center for Advanced Diffusion-Wave and Photoacoustic Technologies (CADIPT), University of Toronto, Toronto, Ontario M5S 3G8, Canada

³ School of Optoelectronic Information, University of Electronic Science and Technology of China, Chengdu 610054, People's Republic of China

E-mail: mandelis@mie.utoronto.ca

Received 21 May 2020, revised 6 September 2020

Accepted for publication 16 September 2020

Published 9 October 2020



CrossMark

Abstract

An anomaly was observed in the heterodyne photocarrier radiometry (HePCR) frequency response of Si wafers in the form of a signal amplitude depression ('dip') accompanied by a 180° phase transition. This phenomenon resembles an electronic notch filter and was investigated experimentally and theoretically by invoking free-carrier-density-wave (CDW) kinetics in generic semiconductor systems. Both homodyne PCR and HePCR signals were obtained from *n*- and *p*-type wafers of different resistivities. Dynamic nonlinear rate-equation models with two bandgap carrier traps were introduced and analytical zeroth and first-order CDW solutions were obtained in the frequency domain. The experimental frequency responses of the HePCR optoelectronic notch phenomenon were found to be in very good agreement with the theory. Characteristic CDW recombination and trap capture and emission characteristic times were obtained and studied as functions of the illuminating laser intensity. The present newly observed HePCR notch phenomenon has revealed a new mechanism of nonlinear contributions due to trap-state-related CDW dynamics in semiconductors superposed on the well-known nonlinear electron-hole recombination interactions that give rise to non-zero HePCR signals. The implications of this notch phenomenon are discussed in terms of its importance in providing physical insights into photocarrier dynamic interactions with traps, leading to identification of active CDW trap-state numbers and precision measurements of their kinetic parameters, carrier capture and emission coefficients, and quantitative trap densities that determine the optoelectronic quality of semiconductors.

⁴ Author to whom any correspondence should be addressed.

Keywords: homodyne, heterodyne, photocarrier radiometry, Si wafers, optoelectronic notch effect, trap densities, capture and emission rates

(Some figures may appear in color only in the online journal)

1. Introduction

Photocarrier radiometry (PCR) [1] is a non-contact and non-destructive spectrally gated frequency-domain dynamic photoluminescence (PL) technique. PCR filters out thermal infrared photon emissions and employs a single-element near-infrared (NIR) sensor to detect photoexcited free-carrier-density-wave (CDW) radiative recombinations in electronic solids such as silicon wafers by recording the amplitude and phase of PL photon-generated PCR signals. PCR has been used for non-contact simultaneous determination of electronic CDW transport parameters in silicon substrates [2–4] and devices [5–7] through best-fitting the amplitude- and phase-frequency responses to appropriate CDW theoretical models [8] by means of suitable multi-parameter fitting procedures. Conventional PCR in which the exciting optical beam is modulated at a single frequency is referred to as ‘homodyne’ (HoPCR). Two-beam heterodyne PCR (HePCR) was introduced [9] to address the need for high-frequency responses required to measure and image recombination lifetimes and other fast photocarrier relaxation processes, primarily through quantitative lock-in carrierography (LIC) [7, 10–12] so as to overcome the limited frame rate of state-of-the-art NIR cameras. The heterodyne technique operates by simultaneously employing two different, yet closely spaced, laser beam modulation frequencies f_1 and f_2 and producing images at the beat frequency $\Delta f = |f_1 - f_2|$ which is compatible with the frame rate of the NIR InGaAs camera. It has been successfully used to characterize the performance of silicon substrates [9–12].

In the process of experimenting with HePCR signals from several p -type Si wafers and solar cells, as well as compound semiconductor materials like CdZnSe wafers, an anomalous behavior in the frequency response was observed in the form of a signal amplitude depression (‘dip’) resembling an electronic notch filter with center frequency f_0 and variable Δf (FWHM) sharpness, also accompanied by a steep 180° phase transition. The f_0 position of the notch centerpoint shifted with laser intensity. Neither the amplitude dip, nor the phase shift appeared in the associated HoPCR responses. Several p - and n -type Si wafers have been examined to-date. As a rule, n -type Si wafers have not exhibited such feature, a fact that nevertheless does not imply a general absence of this behavior with other n -type wafers and it is likely to be the result of not meeting the modulation frequency and free-to-trapped carrier net capture and emission rate resonance condition. In this report, the anomalous behavior is investigated in detail and its physical implications are analyzed with respect to CDW dynamic interactions with trap states in semiconductor Si wafer materials.

2. Theory of HoPCR and HePCR CDW trap-state kinetics

2.1. p -type semiconductor rate equations

A theoretical two-trap frequency-domain kinetic CDW model is developed to interpret the experimental HoLIC and HeLIC amplitude and phase data from semiconductor substrate materials, in the first instance several Si wafers. Two wafers were fully analyzed in this work. The somewhat arbitrary number of two trapping states is justified as a minimum defect configuration on the universal basis of (1) surface trapping (leading to a finite surface recombination velocity), and (2) a minimum of one impurity (doping) state in the bandgap of n - or p -type Si wafers. Additional bandgap states can be added (or, alternatively, the trap structure can be simplified to a single trap state), if warranted by the PCR data. The nonlinear rate equations for majority p -type carrier kinetics (neglecting the minority n -type carriers for simplicity) in a semiconductor exhibiting the anomalous dip behavior with two-trap states are given by:

$$\frac{dp(t)}{dt} = G(t) - \frac{p(t)}{\tau_p} - C_{p1}N_1(t)p(t) + e_{p1}[N_{T1}(t) - N_1(t)] - C_{p2}N_2(t)p(t) + e_{p2}[N_{T2}(t) - N_2(t)], \quad (1a)$$

$$\frac{dN_1(t)}{dt} = -C_{p1}N_1(t)p(t) + e_{p1}[N_{T1}(t) - N_1(t)], \quad (1b)$$

$$\frac{dN_2(t)}{dt} = -C_{p2}N_2(t)p(t) + e_{p2}[N_{T2}(t) - N_2(t)]. \quad (1c)$$

Here $p(t)$ (m^{-3}) is the photogenerated free hole carrier density, $G(t)$ ($\text{m}^{-3} \text{s}^{-1}$) is the optical generation rate, τ_p is the hole recombination lifetime, e_{p1} and e_{p2} (s^{-1}) are the thermal emission rates from traps 1 and 2, respectively, $N_1(t)$ and $N_2(t)$ (m^{-3}) are the trapped carrier densities in the two traps, respectively, C_{p1} and C_{p2} ($\text{m}^3 \text{s}^{-1}$) are the respective trap-state capture coefficients, and N_{T1} and N_{T2} (m^{-3}) are the corresponding trap densities. For homodyne signal generation, the trap densities are considered fixed during the light modulation cycle, as two laser beams are modulated in-phase at the same frequency, whereas for heterodyne signals they are designated to be time-variable, $N_{T1}(t)$ and $N_{T2}(t)$. These dependencies are a departure from the stationary model of intrinsic trap densities in a semiconductor. They emerge only in the heterodyne CDW kinetics as each of the two not-in-phase laser beams acting independently generally modifies the instantaneous trap occupation densities experienced by the other laser beam, thereby changing the number of unoccupied trap states encountered by the latter while both beams impinge on the same semiconductor surface, and thus modifying the effective active (empty)

trap densities. Under harmonic superband-gap optical excitation, photoexcited carrier-density beating can drive the CDW kinetic response at the fundamental frequency (HoPCR) or the sum and difference frequencies (HePCR) and their harmonics which are generated by the coupled nonlinear system of equations (1).

A major analytical advantage of frequency-domain PCR is that nonlinear *differential equation* systems such as equations (1) are reduced to equivalent nonlinear *algebraic equation* systems that can be solved quasi-analytically in a stepwise manner of increasing harmonic frequency multiple orders starting from dc, with $O(1)$ and $O(\omega)$ being the only important solutions under lock-in detection. This is generally impossible to achieve using the time-domain rate equations (1).

2.1.1. HoPCR solutions. The generation rate $G(t) = G(\omega) = 1/2G_0(1 + e^{i\omega t})$ can be described in terms of the fundamental modulation angular frequency $\omega = 2\pi f$

$$G(t) = \sum_{j=-1}^1 G_j e^{ij\omega t}, \quad (2a)$$

$$p(t) = \sum_{j=-\infty}^{\infty} p_j e^{ij\omega t}, \quad (2b)$$

$$N_1(t) = \sum_{j=-\infty}^{\infty} N_{1j} e^{ij\omega t}, \quad (2c)$$

$$N_2(t) = \sum_{j=-\infty}^{\infty} N_{2j} e^{ij\omega t}. \quad (2d)$$

G_0 is the dc component and $G_1 = G_{-1} = G_0/2$. The dependent parameters can be expressed in terms of the fundamental and its harmonics. In equations (2), p_j, N_{1j}, N_{2j} are complex quantities which carry phase information. The negative frequency components are the complex conjugates of the corresponding positive-frequency components. They appear by virtue of expressing the excitation and response sinusoidal optical excitation waveforms in terms of complex exponentials. The zeroth (dc), $O(1)$, and first-order, $O(\omega)$, solutions for the system of equations (1) can be derived through the Fourier series expansions of equations (2):

$$p_0 = G_0 \tau_p, \quad (3a)$$

$$N_{j0} = e_{pj} \tau_{3p}^{(j)} N_{Tj}, \quad (3b)$$

$$p_1(\omega) = \frac{G_0 \tau_p}{(1 + i\omega \tau_p)} \frac{1}{\left\{ 1 + \frac{i\omega \tau_p}{(1 + i\omega \tau_p)} [F_1(\omega) + F_2(\omega)] \right\}}, \quad (3c)$$

$$N_{j1}(\omega) = -F_j(\omega) p_1(\omega), \quad (3d)$$

with the following definitions:

$$\tau_{2p}^{(j)} = \frac{1}{C_{pj} N_{j0}}, \quad (4a)$$

$$\tau_{3p}^{(j)} = \frac{1}{e_{pj} + C_{pj} p_0}, \quad (4b)$$

$$F_j(\omega) = \frac{R_{Tj}}{1 + i\omega \tau_{3p}^{(j)}} \quad (4c)$$

$$R_{Tj} = \frac{\tau_{3p}^{(j)}}{\tau_{2p}^{(j)}}. \quad (4d)$$

Here, $j = 1, 2$ denote the two CDW traps.

2.1.2. HePCR solutions. In the dual-frequency heterodyne mode, the Fourier series for the generation rate and the solutions to equations (1) can be expressed as:

$$G(t) = \sum_{j=-1}^1 G_j e^{ij\omega_1 t} + \sum_{k=-1}^1 G_k e^{ik\omega_2 t}, \quad (5a)$$

$$N_{T1}(t) = N_{T10} + N_{T11} e^{i\omega_1 t} + N_{T11} e^{i\omega_2 t}, \quad (5b)$$

$$N_{T2}(t) = N_{T20} + N_{T21} e^{i\omega_1 t} + N_{T21} e^{i\omega_2 t}, \quad (5c)$$

$$p(t) = \sum_{j=-1}^1 \sum_{k=-1}^1 p_{j,k} e^{i(j\omega_1 t + k\omega_2 t)}, \quad (5d)$$

$$N_1(t) = \sum_{j=-1}^1 \sum_{k=-1}^1 N_{1(j,k)} e^{i(j\omega_1 t + k\omega_2 t)}, \quad (5e)$$

$$N_2(t) = \sum_{j=-1}^1 \sum_{k=-1}^1 N_{2(j,k)} e^{i(j\omega_1 t + k\omega_2 t)}. \quad (5f)$$

Here, j and k indicate response harmonics for excitation at angular modulation frequencies $\omega_1 = 2\pi f_1$ and $\omega_2 = 2\pi f_2$, respectively. Equations (5) show that there are fundamental CDW response frequency components $O(1)$, $O(|\Delta\omega| = |\omega_1 - \omega_2|)$ and $O(\omega_1 + \omega_2)$ generated by nonlinear frequency mixing. According to the foregoing discussion, the two-trap densities are taken as time-variable under heterodyne detection through their dependence on the modulated components which are proportional to the optical generation rate G :

$$N_{T11} = \alpha_1 G_{0,0}, \quad N_{T21} = \alpha_2 G_{0,0}. \quad (5g)$$

Here α_1 and α_2 are coefficients used as fitting parameters. They represent the degree to which trap densities N_{T11} and N_{T21} are time dependent under heterodyne optical excitation. Using equations (5) the solutions to equations (1) can be written as:

$$p_0 = G_0 \tau_p, \quad N_{j(0,0)} = e_{pj} \tau_{3p}^{(j)} N_{Tj0} \quad (6a)$$

$$p_{1,0}(\omega_1) \equiv P(\omega_1), \quad p_{1,0}(\omega_2) \equiv P(\omega_2), \quad (6b)$$

$$N_{j(1,0)}(\omega_1) \equiv N_j(\omega_1), \quad N_{j(1,0)}(\omega_2) \equiv N_j(\omega_2), \quad (6c)$$

$$p_{1,-1}(\Delta\omega) = N_{1(1,-1)}(\Delta\omega) = N_{2(1,-1)}(\Delta\omega) = 0, \quad (6d)$$

$$p_{1,1}(\omega_1 + \omega_2) = - \frac{\sum_{k=1}^2 \frac{iC_{pk}\tau_{3p}^{(k)} g_k(\omega_1 + \omega_2)\tau_p}{1 + i(\omega_1 + \omega_2)\tau_{3p}^{(k)}}}{1 + i(\omega_1 + \omega_2)\tau_p \left(1 + \sum_{k=1}^2 B_{k3}\right)}, \quad (6e)$$

$$N_{j(1,1)}(\omega_1 + \omega_2) = - \frac{C_{pj}\tau_{3p}^{(j)} \left(g_j + N_{j(0,0)}p_{1,1}\right)}{1 + i(\omega_1 + \omega_2)\tau_{3p}^{(j)}}, \quad (6f)$$

with the following definitions:

$$P(\omega_j) = \frac{G_0\tau_p \left(1 + i\omega_j \sum_{k=1}^2 e_{pk}\alpha_k\tau_{2p}^{(k)} F_{jk}\right)}{(1 + i\omega_j\tau_p) \left[1 + \frac{i\omega_j\tau_p}{(1+i\omega_j\tau_p)} \sum_{k=1}^2 F_{k1}\right]}, \quad (7a)$$

$$N_j(\omega_k) = \frac{\tau_{3p}^{(j)}}{1 + i\omega_k\tau_{3p}^{(j)}} \left(e_{pj}N_{Tj1} - \frac{p_{0,1}}{\tau_{2p}^{(j)}}\right), \quad (7b)$$

$$S_j(\omega_j) = \frac{1 + i\omega_j \sum_{k=1}^2 e_{pk}\alpha_k\tau_{2p}^{(k)} F_{kj}}{\left[1 + \frac{i\omega_j\tau_p}{(1+i\omega_j\tau_p)} \sum_{k=1}^2 F_{kj}\right]}, \quad (7c)$$

$$F_{jk}(\omega_k) = \frac{R_{Tj}}{1 + i\omega_k\tau_{3p}^{(j)}}, \quad (7d)$$

$$B_{j3}(\omega_1 + \omega_2) = \frac{R_{Tj}}{1 + i(\omega_1 + \omega_2)\tau_{3p}^{(j)}}, \quad (7e)$$

$$g_j(\omega_1, \omega_2) = N_{j(0,1)}p_{1,0} + N_{j(1,0)}p_{0,1}, \quad (7f)$$

where, R_{Tj} is given by equation (4d) and $j, k = 1, 2$.

In the heterodyne modality, the characteristic times are defined as

$$\tau_{2p}^{(j)} = \frac{1}{C_{pj}N_{j(0,0)}}, \quad (8a)$$

$$\tau_{3p}^{(j)} = \frac{1}{e_{pj} + C_{pj}p_{0,0}}, \quad (8b)$$

where, again, $j = 1, 2$ denote the two CDW traps, respectively.

2.2. *n*-type semiconductor rate equations

The nonlinear rate equations for *n*-type majority carriers in the presence of two carrier traps are:

$$\frac{dn(t)}{dt} = G(t) - \frac{n(t)}{\tau_n} - C_{n1}n(t)[N_{T1} - N_1(t)] + e_{n1}N_1(t) - C_{n2}n(t)[N_{T2} - N_2(t)] + e_{n2}N_2(t), \quad (9a)$$

$$\frac{dN_1(t)}{dt} = C_{n1}n(t)[N_{T1} - N_1(t)] - e_{n1}N_1(t), \quad (9b)$$

$$\frac{dN_2(t)}{dt} = C_{n2}n(t)[N_{T2} - N_2(t)] - e_{n2}N_2(t). \quad (9c)$$

Solutions similar to equations (3) (homodyne) and (6) (heterodyne) can be obtained for the resulting nonlinear algebraic

system of equations under frequency-domain modulation. In this case, the characteristic times are defined as follows:

Homodyne response:

$$\tau_{2n}^{(j)} = \frac{1}{C_{nj}(N_{Tj} - N_{j0})}, \quad (10a)$$

$$\tau_{3n}^{(j)} = \frac{1}{e_{nj} + C_{nj}n_{0,0}}, \quad j = 1, 2 \quad (10b)$$

Heterodyne response:

$$\tau_{2n}^{(j)} = \frac{1}{C_{nj}(N_{Tj0} - N_{j(0,0)})}, \quad (11a)$$

$$\tau_{3n}^{(j)} = \frac{1}{e_{nj} + C_{nj}n_{0,0}}, \quad j = 1, 2 \quad (11b)$$

2.3. HoPCR and HePCR signals

The frequency-domain PCR signal is given by:

$$S(\omega_1, \omega_2) = \sum_{j=-\infty}^{+\infty} \sum_{k=-\infty}^{+\infty} S_{j,k} e^{i(j\omega_1 + k\omega_2)t} \propto p(\omega_1, \omega_2) \times [n(\omega_1, \omega_2) + N_1(\omega_1, \omega_2) + N_2(\omega_1, \omega_2)]. \quad (12)$$

This is a general expression including the possibility of single and dual-frequency excitation waveforms and can be adapted for the PCR signal from *p*-type CDW in either homodyne or heterodyne modality. For HoPCR lock-in detection ($\omega_1 = \omega_2 \equiv \omega$), equation (12) reduces to the simplified form

$$S_{1,0}(\omega) = [N_{11}^*(\omega) + N_{21}^*(\omega)]p_0 + [N_{10} + N_{20}]p_1^*(\omega) + 2p_0p_1^*(\omega). \quad (13)$$

For HePCR lock-in detection at the beat angular frequency $\Delta\omega = |\omega_1 - \omega_2|$

$$S_{-1,1}(\Delta\omega) = [N_{1(0,1)}(\omega_2) + N_{2(0,1)}(\omega_2)]p_{1,0}^*(\omega_1) + [N_{1(1,0)}^*(\omega_1) + N_{2(1,0)}^*(\omega_1)]p_{0,1}(\omega_2) + 2p_{1,0}^*(\omega_1)p_{0,1}(\omega_2). \quad (14)$$

3. Theoretical simulations

3.1. Physical origins of HePCR amplitude dip and phase transition

Figure 1 shows the simulated amplitude and phase behavior of the complex HePCR signal $S_{-1,1}(\Delta\omega)$, equation (14), and the complex HoPCR signal $S_{1,0}(\omega)$, equation (13). A heterodyne depression appears in the amplitude of HePCR at *ca.* 600 Hz accompanied by a steep 180° phase transition, figure 1(b), under a certain combination of characteristic times shown in the figure caption. The other two curves are components A and B of equation (14), where $A = [N_{1(0,1)}(\omega_2) + N_{2(0,1)}(\omega_2)]p_{1,0}^*(\omega_1) + [N_{1(1,0)}^*(\omega_1) + N_{2(1,0)}^*(\omega_1)]p_{0,1}(\omega_2)$, involves products of combinations of trapped and free CDWs oscillating at angular frequencies ω_1

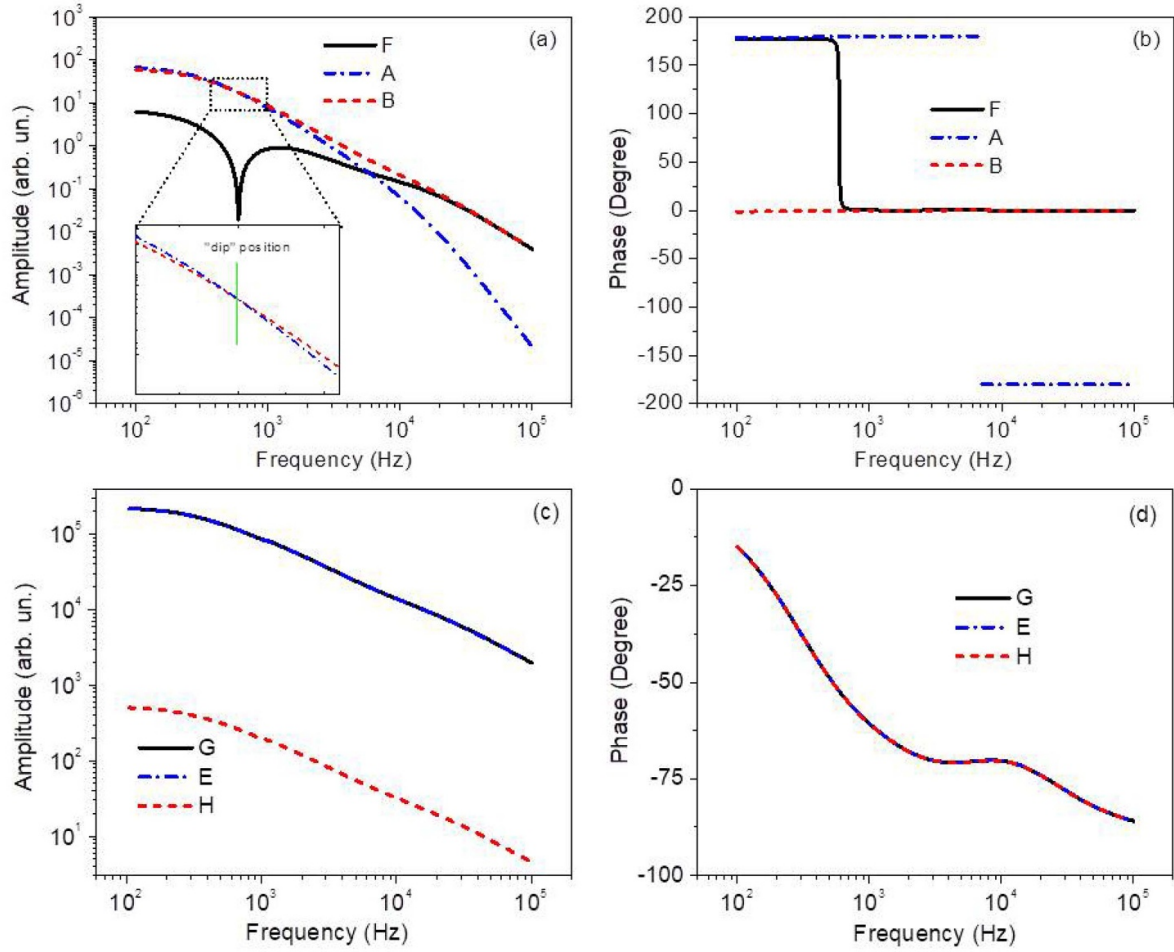


Figure 1. Simulated frequency dependencies of heterodyne PCR components of $S_{-1,1}(\Delta\omega)$ amplitude (a) and phase (b): F: full equation (14); $A = [N_{1(0,1)}^*(\omega_2) + N_{2(0,1)}^*(\omega_2)] p_{1,0}^*(\omega_1) + [(N_{1(1,0)}^*(\omega_1) + N_{2(1,0)}^*(\omega_1))] p_{0,1}(\omega_2)$; $B = 2p_{0,1}(\omega_2) p_{1,0}^*(\omega_1)$. Homodyne PCR $S_{1,0}(\omega)$ amplitude (c) and phase (d): G: full equation (13); $E = [N_{11}^*(\omega) + N_{21}^*(\omega)] p_0 + (N_{10} + N_{20}) p_1^*(\omega)$ and $H = 2p_0 p_1^*(\omega)$. Parameters: $\tau_p = 204 \mu\text{s}$, $\tau_{2p}^{(1)} = 26.1 \mu\text{s}$, $\tau_{2p}^{(2)} = 385 \mu\text{s}$, $\tau_{3p}^{(1)} = 18.3 \mu\text{s}$, $\tau_{3p}^{(2)} = 157 \mu\text{s}$, $N_{T1} = N_{T2} = 1 \times 10^{25} \text{ m}^{-3}$, $G_0 = 2.8 \times 10^{25} \text{ m}^{-3} \text{ s}^{-1}$.

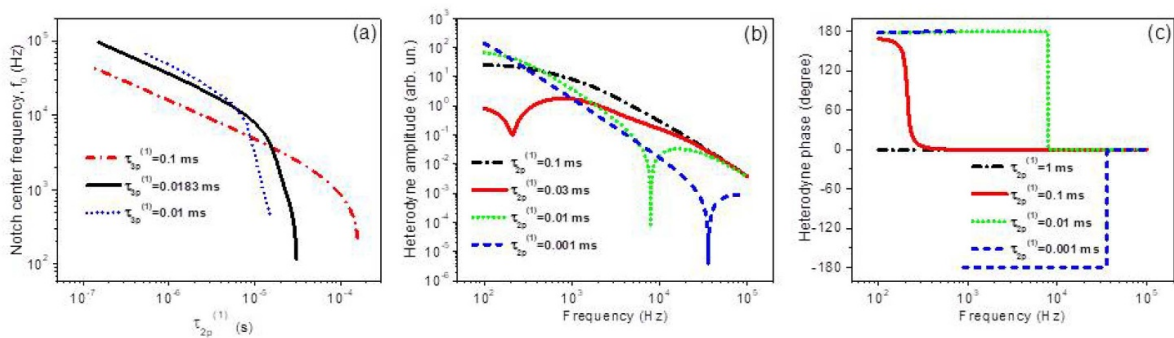


Figure 2. (a) Dependence of PCR amplitude notch center frequency f_0 on relaxation time $\tau_{2p}^{(1)}$ for three values of $\tau_{3p}^{(1)}$; (b) heterodyne amplitude; and (c) phase-frequency dependence showing the shift in dip central positions and phase transitions for four values of $\tau_{2p}^{(1)}$. Other parameters: $\tau_p = 204 \mu\text{s}$, $\tau_{2p}^{(2)} = 385 \mu\text{s}$, $\tau_{3p}^{(1)} = 18.3 \mu\text{s}$, $\tau_{3p}^{(2)} = 157 \mu\text{s}$, $N_{T1} = N_{T2} = 1 \times 10^{25} \text{ m}^{-3}$, $G_0 = 2.8 \times 10^{25} \text{ m}^{-3} \text{ s}^{-1}$.

and ω_2 , and $B = 2p_{0,1}(\omega_2) p_{1,0}^*(\omega_1)$ is the product (mixing) of free-carrier densities driven at those frequencies. Process A involves trapping into, and emission from, trap states which appears overall as an out-of-phase (180°) CDW contribution to the HePCR signal throughout the entire frequency range.

Process B is the direct result of modulated photocarrier mixing by the beating laser beams and its contribution to the HePCR signal occurs in-phase (0°) at the beat angular frequency $\Delta\omega$, again, throughout the entire scanned frequency range. It will be noticed that *only the superposition* of both

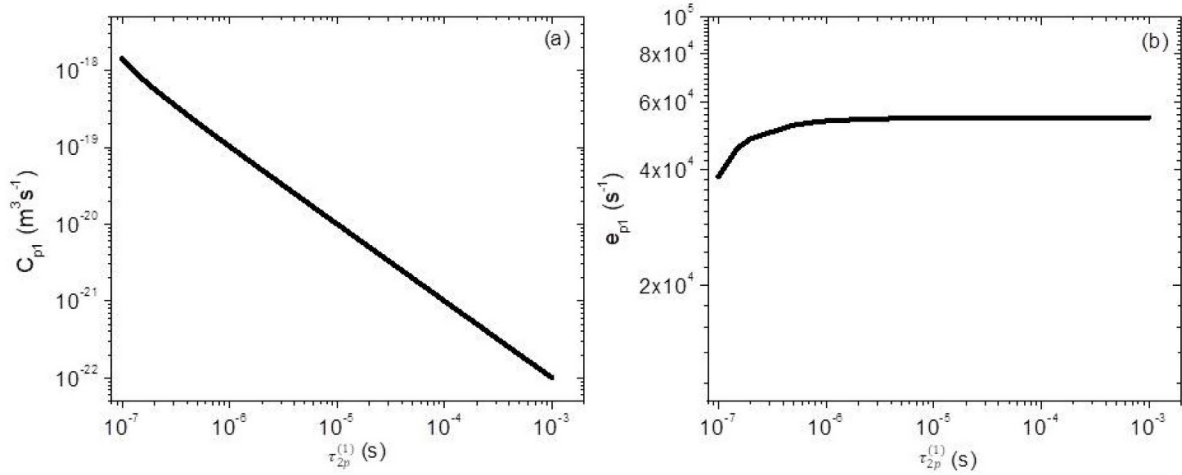


Figure 3. Dependencies of the capture coefficient C_{p1} (a) and emission coefficient e_{p1} (b) on relaxation time $\tau_{2p}^{(1)}$. Other parameters: $\tau_p = 204 \mu\text{s}$, $\tau_{2p}^{(2)} = 385 \mu\text{s}$, $\tau_{3p}^{(1)} = 18.3 \mu\text{s}$, $\tau_{3p}^{(2)} = 157 \mu\text{s}$, $N_{T1} = N_{T2} = 1 \times 10^{25} \text{ m}^{-3}$, $G_0 = 2.8 \times 10^{25} \text{ m}^{-3} \text{ s}^{-1}$.

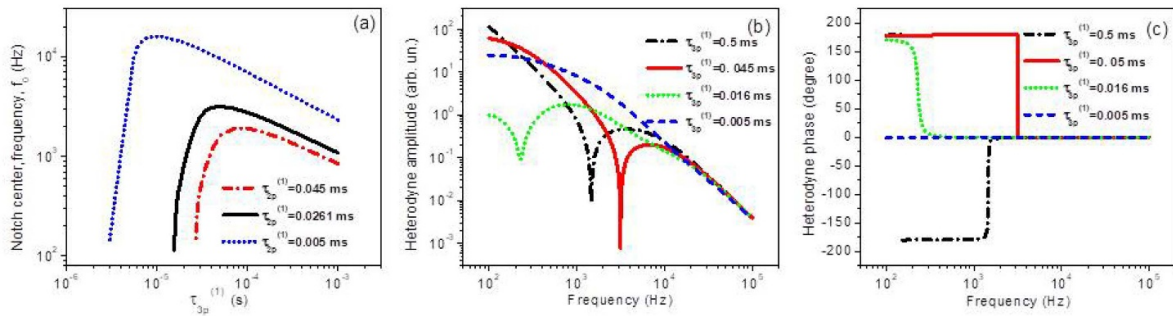


Figure 4. (a) Dependence of PCR amplitude notch center frequency f_0 on relaxation time $\tau_{3p}^{(1)}$ for three values of $\tau_{2p}^{(1)}$; (b) heterodyne amplitude; and (c) phase-frequency dependence showing the shift in dip central positions and phase transitions for four values of $\tau_{3p}^{(1)}$. Other parameters: $\tau_p = 204 \mu\text{s}$, $\tau_{2p}^{(2)} = 385 \mu\text{s}$, $\tau_{3p}^{(1)} = 18.3 \mu\text{s}$, $\tau_{3p}^{(2)} = 157 \mu\text{s}$, $N_{T1} = N_{T2} = 1 \times 10^{25} \text{ m}^{-3}$, $G_0 = 2.8 \times 10^{25} \text{ m}^{-3} \text{ s}^{-1}$.

$S_{-1,1}(\Delta\omega)$ components A + B can generate the sharp amplitude depression and the corresponding phase shift from the 180° phase of A at $f < 600$ Hz to 0° at $f > 600$ Hz. When the two rates leading to processes A and B are superposed, their opposite phases make their relative contributions to the HePCR signal tantamount to one of CDW generation and the other to CDW loss. This behavior is consistent with CDW net contributions to the PCR signal generation through the competing trapped-to-free-carrier release rate described by process A involving the two-trap states, and the free-free-carrier interaction process B, both the results of CDW mixing at the two overlapping angular modulation frequencies ω_1 and ω_2 . Below 600 Hz, process A dominates the HePCR signal contributing to the overall 180° -phase generation rate. Here, process B acts like a CDW loss mechanism. This is followed by the opposite process of free-free-carrier mixing process B which dominates the overall 0° -phase trapped-free-carrier generation rate above 600 Hz. Here, process A acts as the loss mechanism. At the dip frequency, both CDW generation and loss rates are nearly equal and their superposition produces an absence of net CDW for PCR signal generation. In these dynamic optoelectronic processes, the optical

modulation acts like a kinetic resonance window: below the critical frequency, mechanism A dominates at Δf with 180° phase; above that frequency, mechanism B dominates and as a result the phase at Δf abruptly switches to 0° . As a result, the HePCR signal is very sensitive to capture/emission/recombination processes that involve the trap parameters (emission and capture coefficients, trap densities) through the rate equations (1). At high frequencies > 10 kHz, mechanism A appears to become negligible in figure 1(a) and the overall amplitude coincides with that of process B alone. The position of the amplitude notch (dip) and the associated phase transition shifts with τ changes in the values of the characteristic times shown in the caption of figure 1. The beat frequency Δf (1–100 Hz) is much less than the notch center frequency f_0 . Therefore, essentially there is no influence of the values of Δf used experimentally on the position of the ‘dip’ and/or the shape of the frequency response in its neighborhood. This is so because the ‘dip’ appearance is determined by characteristic trap-associated rates $\frac{1}{\tau_{2p}^{(j)}}$, $\frac{1}{\tau_{3p}^{(j)}}$ which remain unaffected unless the sampling rate (beat frequency) becomes commensurate to them.

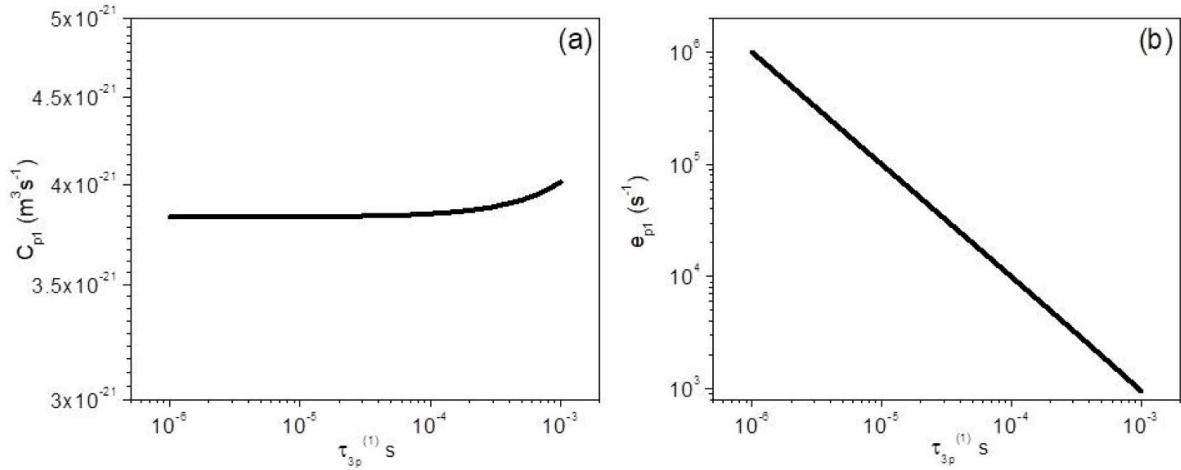


Figure 5. Dependencies of the capture coefficient C_{p1} (a) and emission coefficient e_{p1} (b) on relaxation time $\tau_{3p}^{(1)}$. Parameters: $\tau_p = 204 \mu\text{s}$, at $\tau_{2p}^{(1)} = 26.1 \mu\text{s}$, $\tau_{2p}^{(2)} = 385 \mu\text{s}$, $\tau_{3p}^{(2)} = 157 \mu\text{s}$, $N_{T1} = N_{T2} = 1 \times 10^{25} \text{m}^{-3}$, $G_0 = 2.8 \times 10^{25} \text{m}^{-3} \text{s}^{-1}$.

A decomposition of the HoPCR signal, $S_{1,0}(\omega)$, equation (13), analogous to equation (14), with components $E = [N_{11}^*(\omega) + N_{21}^*(\omega)]p_0 + (N_{10} + N_{20})p_1^*(\omega)$ and $H = 2p_0p_1^*(\omega)$ of the overall signal G , the full equation (13), and the same characteristic time parameters as in figures 2(a) and (b) is shown in figures 2(c) and (d). The homodyne signal exhibits no dip or abrupt phase transition. Here, component E roughly corresponds in physical electronic terms to the heterodyne component A, and component H to B. These components consist of products of zeroth, $O(dc)$, and first-order, $O(\omega)$, terms of products of trapped-carrier and free-carrier densities oscillating at the single angular frequency ω . The major difference between HePCR and HoPCR frequency dependencies is the dip feature and phase transition in the former which can be used for precise identification of the trap-to-free CDW and the free-to-free CDW kinetics below and above the critical frequency, respectively, due to frequency mixing processes. On the contrary, the HoPCR amplitude and phase in this simulation are almost entirely dominated by the trap-to-free CDW kinetics, process E, while the $O(dc)$ and $O(\omega)$ mixing of the free hole CDW is approx. a 400-times-weaker contributor to the PCR signal. The fact that there is mixing of free CDW orders even in the homodyne signals is due to the nonlinearity of the governing rate equations (1) (or (9)).

3.2. Amplitude dip center frequency dependence on trap kinetic parameters

To investigate more closely the dependence of the HePCR dip center frequency f_0 position on various trap-related parameters and characteristic time constants, figure 2(a) shows the dependence of the f_0 position on $\tau_{2p}^{(1)}$ for various values of $\tau_{3p}^{(1)}$. Increasing $\tau_{2p}^{(1)}$ very sensitively shifts f_0 to lower values. This is a manifestation of the resonance character of the CDW generation rate (PCR modulation frequency) matching the

trap carrier capture rate inherent in the definition of $1/\tau_{2p}^{(1)}$, equation (8a). Equation (8b) shows that the net trap-emission and free-carrier-capture rate $1/\tau_{3p}^{(1)}$ also contributes to the dip frequency, although not as sensitively as $\tau_{2p}^{(1)}$: In general, increasing $\tau_{3p}^{(1)}$ decreases the dip frequency in a manner which evokes a similar rate matching relation of the modulation frequency with a more complicated characteristic kinetic rate as indicated by equation (3c) through the factors $F_j(\omega)$.

The foregoing discussion on the physical origins of the dip concluded that its center frequency location depends on the values of the various characteristic times associated with the trap states in the model and the free CDW generation and trapping or recombination rate. Figures 2(b) and (c) explore the frequency dependence, f_0 , of the HePCR amplitude dip center position and the associated phase transition on the value of $\tau_{2p}^{(1)}$. It is clear that decreasing $\tau_{2p}^{(1)}$ shifts f_0 and the associated phase transitions to higher frequencies. For the largest plotted $\tau_{2p}^{(1)} = 0.1$ ms, the amplitude dip occurs at a frequency below the minimum 100 Hz and cannot be observed in figure 2(a). According to the definition of $\tau_{2p}^{(1)}$, this dip shift trend is consistent with the influence of the CDW trap capture rate discussed in conjunction with figure 1. Figure 2(c) shows that for $\tau_{2p}^{(1)} = 0.001$ ms, the phase transition from $+180^\circ$ to 0° switches to an opposite transition from -180° to 0° . This effect is observed for short $\tau_{2p}^{(1)}$ values for which the phase transition behavior is opposite to that shown in figure 1(b). Its origin is discussed below in the study of the effects of $\tau_{3p}^{(1)}$ values in the HePCR frequency responses.

The capture lifetime $\tau_{2p}^{(1)}$ decreases drastically with increasing capture coefficient when all other relaxation times remain fixed, figure 3(a). $\tau_{2p}^{(1)}$ also depends on e_{p1} with the dependence being mediated through the respective dependence of $N_{1(0,0)}$ on e_{p1} in the $\tau_{2p}^{(1)}$ definition,

equation (8a). Figure 4(b) shows that for the $\tau_{2p}^{(1)}$ behavior of figure 3(a), the emission coefficient increases only slightly. The ultimate importance of these figures lies in that they show that $\tau_{2p}^{(1)}$ is most sensitive to changes in the trapping rate of free carriers in trap # 1 with density N_{T10} . As a general rule, it should be mentioned that all relaxations times are interdependent through their definitions in terms of the system parameters e_{p1} , C_{p1} , $N_{1(0,0)}$, and p_0 according to equations (6a) and (8a, 8b). Equation 8(b) shows that for fixed $\tau_{3p}^{(1)}$ and $p_{0,0}$ as in figure 3(b), a decreasing emission rate e_{p1} must be compensated by an increasing capture coefficient C_{p1} . Figure 4(b) indicates that for large $\tau_{2p}^{(1)}$ values, e_{p1} saturates as the maximum $\tau_{3p}^{(1)}$ value set in the simulation is reached.

Figure 4(a) shows the behavior of f_0 as a function of the characteristic time $\tau_{3p}^{(1)}$ with $\tau_{2p}^{(1)}$ as a parameter. Although the general trend of monotonically increasing f_0 with decreasing $\tau_{2p}^{(1)}$ above the peak of this curve is consistent with figure 2(b), nevertheless, the value f_0 is not always monotonic with $\tau_{3p}^{(1)}$, a fact that also becomes apparent in figure 4(b). It is also interesting to note in figures 4(b) and (c) that the amplitude dip and the phase transition for the curve with $\tau_{3p}^{(1)} = 5 \times 10^{-6}$ s lies below the minimum frequency displayed. The amplitude dip and phase transition $+180^\circ$ to 0° f_0 increases monotonically in increasing sequence for $\tau_{3p}^{(1)}$ values 5×10^{-6} s, 1.6×10^{-5} s, and 4.5×10^{-5} s. However, this pattern breaks down for the case $\tau_{3p}^{(1)} = 5 \times 10^{-4}$ s where f_0 appears between those with $\tau_{3p}^{(1)} = 1.6 \times 10^{-5}$ s and 4.5×10^{-5} s. To highlight this anomalous behavior, the phase transition at this $\tau_{3p}^{(1)}$ value occurs instead between -180° and 0° . Toward the high-frequency end, all curves in figure 4(a) converge to the same amplitude which has been identified with the dominant free-free-carrier mixing process B in section 3.1. A glance at the expression for component A shows that the sign of the phase can change from $+180^\circ$ to -180° when the terms with complex conjugation dominate those without it. These conditions are also present for short $\tau_{2p}^{(1)}$ characteristic times in figure 2(c). Therefore, it is concluded that the terms associated with the trapped-to-free-carrier release rate described by process A involving one or both trap states sometimes lead, and other times lag, the free-free-carrier interaction process B. Switches in the relative weights of these dynamic CDW processes with frequency changes are responsible for the non-monotonicity of the dip f_0 position and the phase transitions exhibited in figures 4(a)–(c). The opposite trends between the effects of $\tau_{2p}^{(1)}$ and $\tau_{3p}^{(1)}$ in determining the dominant dynamic carrier processes are also illustrated in figures 5(a) and (b) where the behaviors of capture and emission coefficients of trap # 1 as functions of $\tau_{3p}^{(1)}$ are opposite to those exhibited in figures 3(a) and (b), as functions of $\tau_{2p}^{(1)}$. Simulations involving trap # 2 yield trends and behaviors similar to those encountered with trap # 1, therefore they are not detailed here. The overall semiconductor behavior is due to the superposition of the behaviors of the two-trap states.

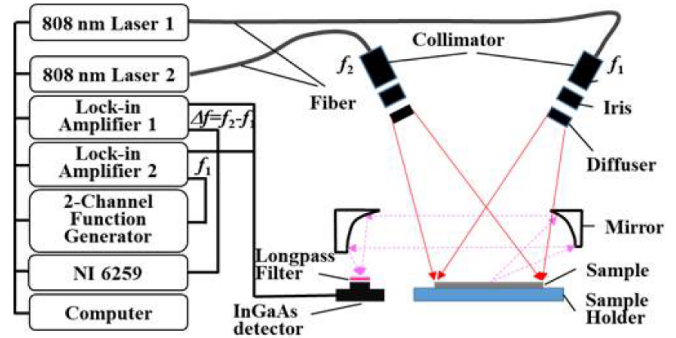


Figure 6. Diagram of HoPCR and HePCR system. Two photoexcitation lasers are modulated at angular frequencies ω_1 and ω_2 with $\omega_1 = \omega_2$ for HoPCR and the beat frequency difference $\Delta\omega = |\omega_1 - \omega_2|$ for HePCR to which the two lock-in amplifiers are tuned.

4. Experimental, results and discussion

A schematic of the experimental PCR system is shown in figure 6. In this system, the beams of two 808-nm fiber-coupled lasers were first collimated, then spread and homogenized by micro-lens arrays to form a 2×2 cm² illuminated area. The mean value of each laser beam intensity was 1.1 W cm⁻² at maximum operating emission. Intensity scans were made by adjusting an iris that was placed in the path of each laser beam. The two beams were square-wave modulated using a two-channel function generator in the range 0.1–100 kHz for optimal signal-to-noise ratio (SNR). A long-pass filter LP-1000 nm from Spectrogon was used to prevent the excitation laser beams from interfering with the InGaAs NIR detector. Diffuse radiative recombination-induced signals were collected and collimated with two off-axis paraboloidal mirrors focused on the detector. The detected signal was demodulated using two lock-in amplifiers referenced at the common frequency $f_1 = f_2$ in the case of HoPCR, and at the (beat) frequency difference $\Delta f = |f_1 - f_2|$ in the case of HePCR. The frequency difference Δf between the two beams used in the HePCR measurements was 10 Hz for all experiments.

Several Si wafers (including solar cells, not presented in this study) were measured and the detailed results from two wafers are presented here to illustrate the frequency notch phenomenon: one *p*-type sample (diameter: 150 mm, resistivity: 28–48 Ω cm, thickness: 675 μ m), and one *n*-type sample (diameter: 100 mm, resistivity: 0.001–0.005 Ω cm, thickness: 500 μ m). For all wafers, HoPCR and HePCR measurements were performed. Frequency scans with laser beam intensity as a parameter were also made. The homodyne and heterodyne signals were best fitted to the theory using the *p*-type and *n*-type two-trap CDW theoretical kinetic models developed in section 2. Figures 7 and 8 show the HoPCR amplitudes and phases for the aforementioned *p*-type and the *n*-type wafers, respectively, with laser beam intensity as a parameter. These signals exhibited high SNR and reproducibility in the 100 Hz–100 kHz range. Figure 7(a) shows the typical noise floor in the experiments at all frequencies. The measurement results exhibit the expected amplitude decrease with increasing

frequency [1] above the ‘knee’. Figures 7 and 8 also show best fits of the data to equation (13) for $S_{1,0}(\omega)$ with excellent agreement between experiment and theory.

Figures 9 and 10 show the HePCR amplitudes and phases corresponding to the abovementioned wafers. Figure 9(a) shows the noise floor for these measurements which exhibited high SNR and reproducibility only in the 100 Hz–10 kHz range. In all cases, the HePCR signals were approximately one order of magnitude lower than the corresponding HoPCR signals. It is clear from figures 9(a) and 10(a) that the p -type wafer exhibits the amplitude notch effect and steep phase transition, whereas the n -type wafer does not. It should be noted that the experimental results exhibited the anomalous behavior for several p -type wafers but *not* for any of the examined n -type wafers. This difference cannot be conclusive as being due to differences in doping type, but is likely to be the result of the net carrier trapping/emission rates not meeting the modulation frequency matching (resonance) condition encountered with p -type wafers and it needs further investigation. Figures 9(a) and 10(a) show that in the p -type wafer the notch effect appears at an intermediate range intensities with f_0 and the phase transition range shifting to higher frequencies with decreasing intensity. Careful inspection of the amplitude and phase trends makes it clear that for the highest relative intensity (0.9 max), these features occur at frequencies much lower than the lowest experimental frequency (100 Hz), whereas for intensities below 0.5 max they should start to appear above 10 kHz but may be entirely concealed within the noise floor. The p -type wafer phase originates at -180° at frequencies below f_0 before undergoing a rapid transition/lead to near 0° at, and above that frequency as predicted by the theoretical model of section 2. For the n -type wafer that exhibits no HePCR notch effect, the heterodyne phase remained fixed at 0° , as expected from the very small difference in frequency Δf between the two beating laser beams. For this Si wafer and several other n - and p -type materials the carrier kinetic properties of which do not produce the notch phenomenon, the amplitude vs. frequency curve shapes, figure 9(b), are similar to their associated HoPCR amplitudes. Because of this resemblance to the well-known nonlinear HoPCR frequency response the origin of which is rooted in the electron-hole CDW interaction as a result of single-frequency optical modulation [13], had the present notch phenomenon not been discovered through the HePCR response, there would have been no indication of the *additional nonlinear* contributions to this modality by trap-state-related dynamics in semiconductors. In summary, it was found that the fundamentally nonlinear character of heterodyne signal generation naturally amplifies the HePCR response dependence on nonlinear rate kinetics of carrier capture into, and emission from, optoelectronic traps, regardless of the presence or not of a notch effect superposed on the fundamental electron-hole interaction based nonlinear HePCR signal generation processes. As such, the present notch phenomenon has no literature precedence. In what follows it is shown that it contributes substantially to our ability to identify and study trap-state dynamics and non-destructively characterize optoelectronic semiconductor materials and devices.

Best-fitting the HePCR theory to the data of figures 9 and 10 yielded measurements of the relevant crucial physical kinetic parameters: band-to-band recombination lifetimes, trap-emission rates, carrier capture coefficients and total trap densities. These parameters were further investigated as functions of laser beam intensity (and thus CDW generation rate) and its effects on the various characteristic times shown in equations (4), (8), (9) and (10) which are defined in terms of those parameters. The mean characteristic time (lifetime) measurements derived from five repeated best-fitted HePCR and HoPCR signal results were calculated and are shown in figures 11 and 12, respectively. The theoretical best fits showed excellent agreement with the experiment results, figures 7–10. Uniqueness analysis of the HoPCR signal-derived characteristic times confirmed them to be unique in the entire experimental time range (1–1000 μ s). It was concluded that the nonlinear two-trap model (p -type and n -type) was necessary and sufficient to describe the CDW kinetics in both HoPCR and HePCR modalities. To first order, the two-trap model can be associated with surface recombination trap sites and bandgap impurity states. At room temperature most of these doping states are expected to be empty at equilibrium, but in the highly non-equilibrium steady state of homodyne and heterodyne optical excitation, with large numbers of excess free carriers roaming at or near the bandedge, empty shallow impurity states may act as shallow traps, giving rise to the notch phenomenon at (resonant) frequencies at which the excitation rate equals the trapping rate. For the HePCR signals, the p -type two-trap model with time-variable trap densities, equations (1) and (5g), was used as discussed in section 2.1.

5. CDW trap parameter extractions

The laser intensity dependence of the characteristic times can be used for extracting the main trap parameters, such as emission and capture coefficients and trap concentrations. The emission coefficient, e_m , and the capture coefficient, C_m , although formally independent of laser intensity, nevertheless, may depend on the latter due to increasing wafer temperature with intensity. Here m indicates p for the p -type silicon wafer and n for the n -type silicon wafer. Net trap charging with changing occupation may be another factor affecting these parameters. Under these conditions, e_m and C_m may be expressed as [14]:

$$e_m \propto T^2 e^{-\frac{\Delta E}{kT}} \approx a_1 + a_2 G_0 + a_3 G_0^2, \quad (15)$$

$$C_m \propto T^{0.5} \approx a_4 G_0^{0.5}, \quad (16)$$

where T is absolute temperature, and a_1 , a_2 , a_3 , and a_4 are coefficients to be determined. It was experimentally found that the temperature in the illuminated area increases proportionally with laser intensity up to 335 K.

The e_{pi} , C_{pi} , and N_{Ti} dependencies of $\tau_{2p}^{(i)}$ and $\tau_{3p}^{(i)}$ were extracted from equations (6a), (8a), (8b), (15), and (16) in simultaneous best fits for the evaluation of these parameters. The

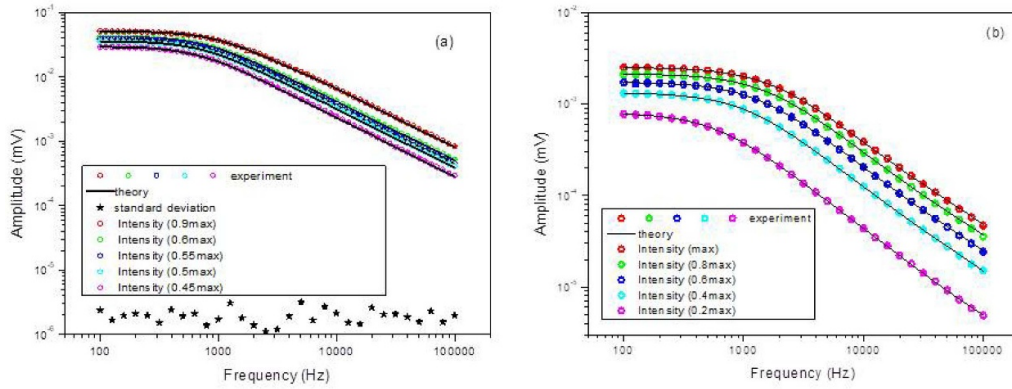


Figure 7. HoPCR amplitude-frequency scans for various intensities: (a) *p*-type wafer; (b) sample *n*-type wafer.

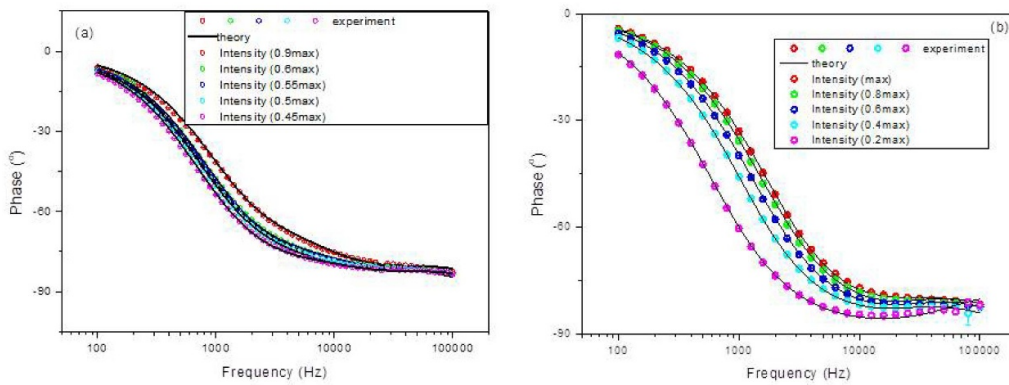


Figure 8. HoPCR phase-frequency scans at various intensities: (a) *p*-type wafer; (b) sample *n*-type wafer.

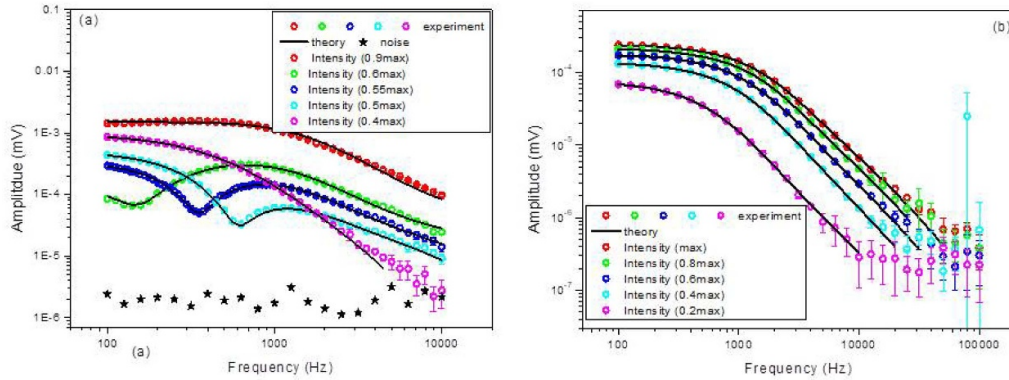


Figure 9. HePCR amplitude-frequency scans at various intensities: (a) *p*-type wafer; (b) sample *n*-type wafer.

e_{pi} and C_{pi} values for the *p*-type wafer, calculated from the HoPCR and HePCR relaxation time measurements of figures 11 and 12, are shown in figures 13(a) and (b), respectively. Both modalities show that the two coefficients increase with intensity as expected from wafer laser heating. The emission and capture coefficients for traps #1 and #2 differ in value and also differ between HoPCR and HePCR measurements. Similar results and trends were obtained from the *n*-type wafer, figure 14. In addition, the calculated differences between the parameters of the two traps were found to be much higher for the *p*-type wafer than for the *n*-type wafer.

The derived parameter values using the experimental generation rate $G_0 = 3.7 \times 10^{25} \text{ m}^{-3} \text{ s}^{-1}$ are summarized in table 1 for the *p*-type wafer and for the *n*-type wafer. From the viewpoint of the optoelectronic quality characterization of the wafer, the most important parameters are the values of N_{T1} and N_{T2} , the residual trap densities. As mentioned in section 2.1, the HePCR kinetic CDW rate equations involve time dependence of these parameters, whereas HoPCR values are assumed stationary which is the standard assumption for intrinsic trap densities interacting with a single superband-gap optical beam in a semiconductor. As a result, the effective

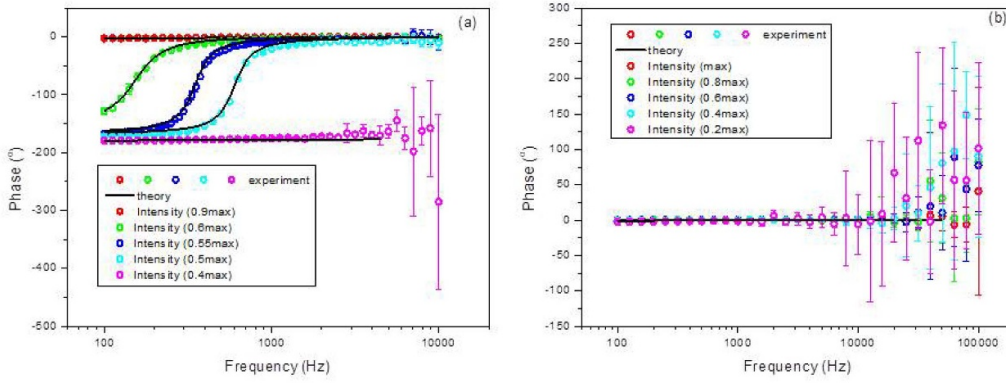


Figure 10. HePCR phase-frequency scans at various intensities: (a) *p*-type wafer; (b) sample *n*-type wafer.

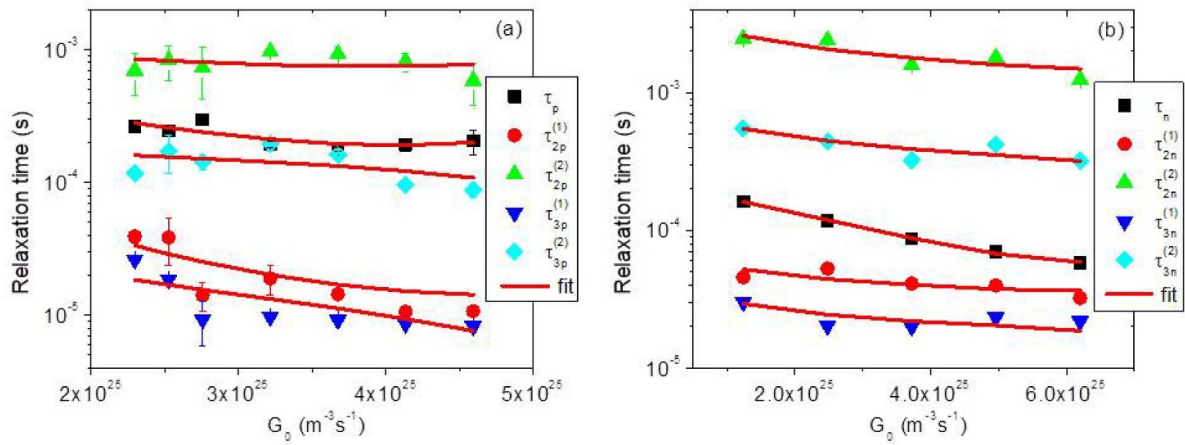


Figure 11. Dependence of best-fitted relaxation times on intensity from HePCR frequency scans: (a) *p*-type wafer; (b) sample *n*-type wafer.

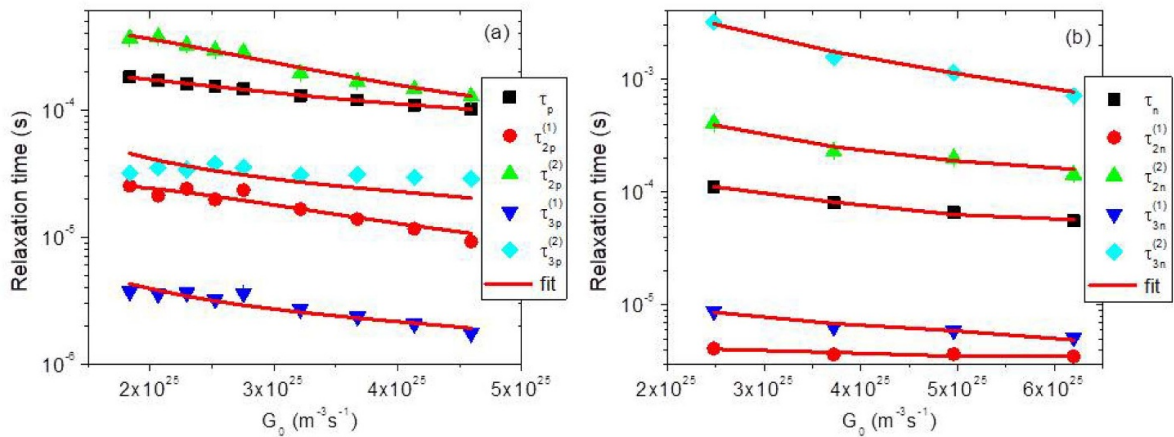


Figure 12. Dependence of best-fitted relaxation times on intensity from HoPCR frequency scans: (a) *p*-type wafer; (b) sample *n*-type wafer.

(empty) trap densities in table 1 vary between the two modalities by up to factors of 3–24 for the two wafers. Other parameters leading to those results are also different. The general trends for lower HePCR trap density measurements are reasonable on physical grounds: The first (leading) laser beam tends to fill up trap states following band-to-band photogeneration of free carriers, so that carriers generated by the second (lagging)

beam encounter increased state occupation which, in turn, results in smaller effective trap densities for both types of wafers. For the *p*-type wafer, excess band-to-band de-excitations due to contributions from trapped carriers captured after excitation by the leading beam, result in smaller valence band free hole densities available for de-excitations following the lagging beam, and thus exhibit longer recombination

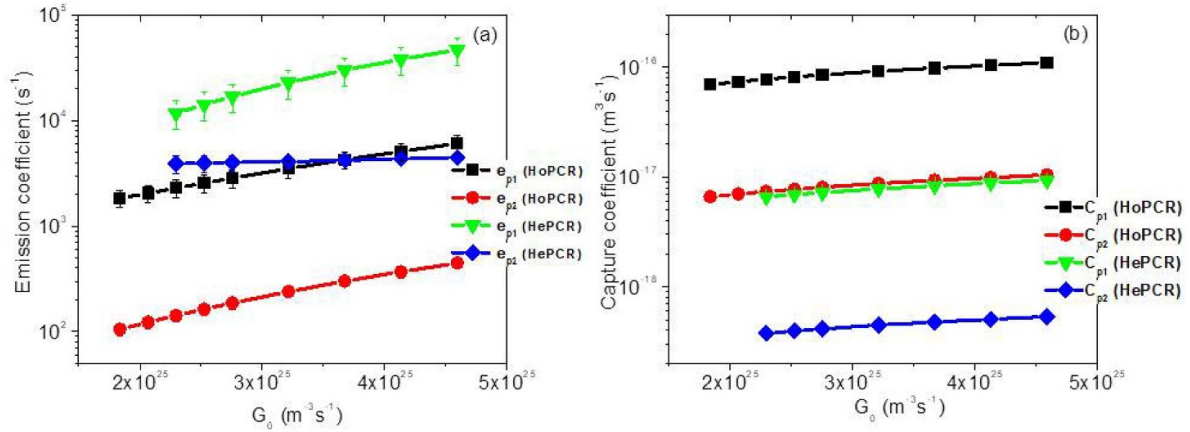


Figure 13. Generation rate dependencies of derived emission coefficient (a) and capture coefficient (b) as results of inverse best-fitting to the HoPCR and HePCR relaxation time dependences of p -type wafer.

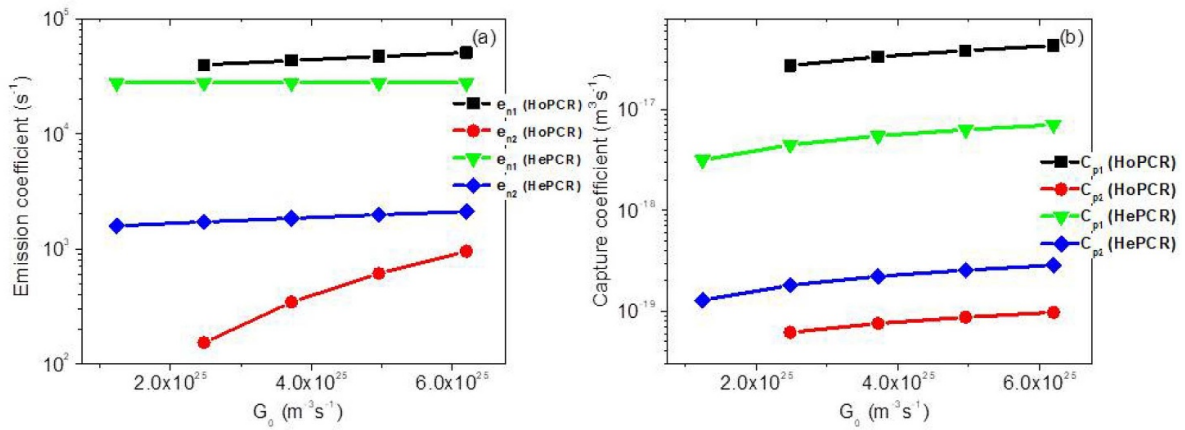


Figure 14. Generation rate dependencies of derived emission coefficient (a) and capture coefficient (b) as results of inverse best-fitting to the HoPCR and HePCR relaxation time dependences of sample n -type wafer.

Table 1. Evaluated parameters of p -type wafer and n -type wafer at $3.7 \times 10^{25} \text{ m}^{-3} \text{ s}^{-1}$ generation rate. Subscript m stands for p (p -type silicon wafer) or for n (n -type silicon wafer).

Parameter	p -type wafer. homodyne	p -type wafer. heterodyne	n -type wafer. homodyne	n -type wafer. heterodyne
τ_m (μs)	119.60 ± 0.03	179.0 ± 5.8	80.700 ± 0.001	86.600 ± 0.003
$\tau_{2m}^{(1)}$ (μs)	13.82 ± 0.03	14.4 ± 1.1	3.630 ± 0.001	41.000 ± 0.003
$\tau_{2m}^{(2)}$ (μs)	166.90 ± 0.05	921 ± 65	229.00 ± 0.01	1579.00 ± 0.05
$\tau_{3m}^{(1)}$ (μs)	2.360 ± 0.003	9.20 ± 0.57	63.900 ± 0.001	19.900 ± 0.001
$\tau_{3m}^{(2)}$ (μs)	30.90 ± 0.01	161.0 ± 3.6	1564.0 ± 0.1	323.00 ± 0.01
e_{m1} (s^{-1})	$(4.3 \pm 0.8) \times 10^3$	$(3.0 \pm 0.9) \times 10^4$	$(4.300 \pm 0.002) \times 10^4$	$(2.80 \pm 0.01) \times 10^4$
e_{m2} (s^{-1})	$(3.0 \pm 0.4) \times 10^2$	$(4.2 \pm 0.5) \times 10^3$	$(3.4 \pm 0.5) \times 10^2$	$(1.80 \pm 0.01) \times 10^3$
C_{m1} ($\text{m}^3 \text{ s}^{-1}$)	$(9.90 \pm 0.02) \times 10^{-17}$	$(8.3 \pm 0.1) \times 10^{-18}$	$(3.40 \pm 0.01) \times 10^{-17}$	$(5.5 \pm 0.01) \times 10^{-18}$
C_{m2} ($\text{m}^3 \text{ s}^{-1}$)	$(9.30 \pm 0.07) \times 10^{-18}$	$(4.8 \pm 0.5) \times 10^{-19}$	$(7.50 \pm 0.01) \times 10^{-20}$	$(2.20 \pm 0.04) \times 10^{-19}$
N_{T1} (m^{-3})	$(7.5 \pm 1.6) \times 10^{22}$	$(2.20 \pm 0.01) \times 10^{22}$	$(2.60 \pm 0.01) \times 10^{22}$	$(7.400 \pm 0.022) \times 10^{21}$
N_{T2} (m^{-3})	$(8.5 \pm 0.8) \times 10^{22}$	$(5.2 \pm 0.6) \times 10^{21}$	$(8.80 \pm 0.01) \times 10^{22}$	$(3.50 \pm 0.03) \times 10^{21}$

lifetime than in HoPCR carrier kinetics. For the n -type wafer there is little difference between homodyne and heterodyne recombination lifetimes. The pair of proportionality coefficients α_1 and α_2 (one for each trap, equation 5g) when treated as adjustable quantities for data fitting, show

how immune the residual trap densities are to laser beam induced fluctuations, from no effect ($\alpha = 0$) to considerable effect ($\alpha > 0$ or < 0). The use of the two parameters α_1 and α_2 was shown to be a sensitive measure of the (in)dependence of trap densities (from) on laser HePCR

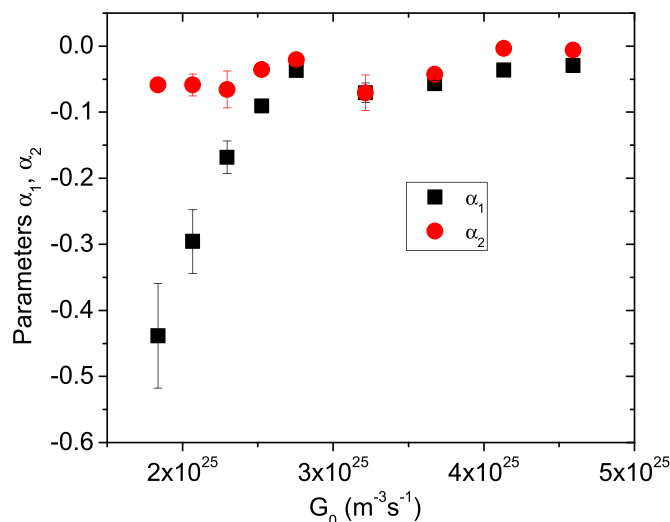


Figure 15. Dependence of best-fitted coefficients α_1 and α_2 on intensity from HePCR frequency scans for *p*-type wafer.

excitation of free carriers. The homodyne-derived parameters should therefore serve as a reference for how heterodyne excitation affects them. Unlike the homodyne approach where trap densities are expected to be a fixed sample property, the heterodyne method's cross-beam interaction process is such that effective trap densities may indeed be a function of laser parameters. The fitted coefficients for the *p*-type wafer are shown in figure 15. It is seen that one of the values, α_2 , corresponding to trap# 2 is essentially equal to zero for all laser intensities. This renders the density of trap # 2 independent of photocarrier density and therefore an intrinsic property of the material. On the other hand, the coefficient α_1 is negative up to $2.8 \times 10^{25} \text{ m}^{-3} \text{ s}^{-1}$ generation rate, most likely due to efficient emptying of the trap state at intermediate intensities. At high intensities/generation rates $>2.8 \times 10^{25} \text{ m}^{-3} \text{ s}^{-1}$, trap # 1 is likely to become entirely empty and thus its full capturing density is restored and becomes an intrinsic material property, independent of laser intensity, with $\alpha_1 \approx 0$.

6. Conclusions

A newly discovered electronic notch type of an anomaly in the HePCR frequency response of Si wafers, solar cells and some compound semiconductor materials was presented. This phenomenon was investigated in detail experimentally with *p*- and *n*-type Si wafers and theoretically by means of non-linear trap-state dynamic responses to optically generated heterodyne frequency-domain beat processes in generic semiconductor systems. The notch features (amplitude dip and 180° phase transition) appear only in the HePCR modality and not in conventional HoPCR frequency scans. Their importance lies in that they add physical insight to photocarrier dynamic optoelectronic interactions with traps in semiconductors and thus enable the non-contacting, non-destructive identification and measurement of trap-state kinetic parameters, including numbers of active trap states, characteristic trap-associated

times (lifetimes) and capture and emission coefficients of photoexcited CDWs. It was shown that these dynamic trap properties can be used to measure the active trap densities, quantitative measurements that are very important in determining the optoelectronic quality of wide ranges of semiconductor materials and devices.

Acknowledgments

The authors are grateful to the Natural Sciences and Engineering Research Council of Canada (NSERC) for a Discovery grant to A. M., and to the Canada Research Chairs program. Y. Q. Song acknowledges the NSFC (Grant No. 11672224) and financial support from the program of China Scholarships Council (201806285044). A. Mandelis is grateful to CFI-ORF for John R. Evans Leaders Fund (JELF) grant.

ORCID iDs

Alexander Melnikov  <https://orcid.org/0000-0002-0020-9862>

Qiming Sun  <https://orcid.org/0000-0003-1184-3719>

References

- [1] Mandelis A, Batista J and Shaughnessy D 2003 *Phys. Rev. B* **67** 205208
- [2] Batista J, Mandelis A and Shaughnessy D 2003 *Appl. Phys. Lett.* **82** 4077
- [3] Li B, Shaughnessy D, Mandelis A, Batista J and Garcia J 2004 *J. Appl. Phys.* **96** 186
- [4] Liu J, Song P, Qin L, Wang F and Wang Y 2015 *Acta Phys. Sin.* **64** 087804
- [5] Zhang Y, Melnikov A, Mandelis A, Halliop B, Kherani N P and Zhu R 2015 *Rev. Sci. Instrum.* **86** 033901
- [6] Song P, Liu J Y, H M Y, Oliullah M, Wang F and Wang Y 2016 *Nucl. Instrum. Methods Phys. Res. B* **383** 171

- [7] Sun Q M, Melnikov A, Mandelis A and Pagliaro R H 2018 *Appl. Phys. Lett.* **112** 012105
- [8] Mandelis A 2001 *Diffusion-Wave Fields: Mathematical Methods and Green Functions* (New York: Springer) ch 9 pp 584–708
- [9] Melnikov A, Chen P, Zhang Y and Mandelis A 2012 *Int. J. Thermophys.* **33** 2095
- [10] Song P, Melnikov A, Sun Q M, Mandelis A and Liu J Y 2019 *J. Appl. Phys.* **125** 065701
- [11] Hu L, Mandelis A and Sun Q 2019 *IEEE J. Photovolt.* **9** 132–8
- [12] Sun Q M, Melnikov A and Mandelis A 2016 *Phys. Status Solidi a* **213** 405–411
- [13] Tolev J, Mandelis A and Pawlak M 2007 *J. Electrochem. Soc.* **154** H983–94
- [14] Schroder D K 1998 *Semiconductor Material and Device Characterization* 2nd edn (New York: Wiley) ch 5 pp 267–336